α-ϵ transition pathway of iron under quasihydrostatic pressure conditions

N. Ishimatsu,* Y. Sata, and H. Maruyama
Department of Physics, Graduate School of Science, Hiroshima University, 1-3-1 Kagamiyama, Higashihiroshima, Hiroshima 739-8526, Japan

T. Watanuki
Condensed Matter Science Division, Quantum Beam Science Directorate, Japan Atomic Energy Agency (JAEA), Sayo, Hyogo 679-5148, Japan

N. Kawamura and M. Mizumaki
Japan Synchrotron Radiation Research Institute (JASRI), SPring-8 1-1-1 Kouto, Sayo-cho, Sayo-gun, Hyogo 679-5198, Japan

T. Irifune
Geodynamics Research Center (GRC), Ehime University, 2-5 Bunkyo-cho, Matsuyama 790-8577, Japan

H. Sumiya
Advanced Materials R&D Laboratories, Sumitomo Electric Industries, 1-1-1 Koyakita, Itami, Hyogo 664-0016, Japan
(Received 31 March 2014; revised manuscript received 23 June 2014; published 17 July 2014)

We have carefully investigated the α-ϵ transition pathway of iron under quasihydrostatic pressures. For this purpose, combined measurements of extended x-ray absorption fine structure (EXAFS) and x-ray magnetic circular dichroism at the Fe K edge were performed using a helium pressure-transmitting medium. Collapse of the ferromagnetism simultaneously occurs with the α-ϵ structural transition, which is in contrast to the scenario that the transition is driven by the pressure-induced instability of the ferromagnetism in α phase of iron. We conclude that shear stress is important to initiate the α-ϵ transition. Our model to fit the EXAFS profile demonstrates that the local atomic arrangement in ϵ phase is slightly distorted due to unfinished shuffle motion, whereas shear motion finishes at the beginning of the transition.

DOI: 10.1103/PhysRevB.90.014422 PACS number(s): 81.30.Kf, 61.05.cj, 61.50.Ks, 75.50.Bb

I. INTRODUCTION

Iron undergoes a pressure-induced bcc (α) to hcp (ϵ) transition at about 14 GPa. The transition has attracted great interest after its discovery by Bancroft in 1953 [1], because the ϵ phase of iron is one of the important materials for both solid state physics and geosciences. The ferromagnetism in iron is suppressed during the transition, and the ϵ phase is considered to be nonmagnetic or antiferromagnetic. The α-ϵ transition is a martensitic transformation, wherein the reconstructive structural transition occurs via shear and shuffle motion of the $(110)_\alpha$ planes. Although various transition pathways of iron have been proposed by many researchers, the driving mechanism of the structural and magnetic transitions is not fully understood. The α and ϵ phases have equal enthalpies at about 10 GPa [2]; however, a pronounced barrier exists between the two phases in the enthalpy surface. The application of pressure up to 50 GPa, which is considerably higher than the experimental value, is predicted for the excitations beyond the barrier at room temperature [2]. Therefore an understanding of how to overcome the barrier is a major problem of the α-ϵ transition.

The first scenario is magnetism-driven transition due to the thermodynamical instabliliy of the ferromagnetism in the α phase under pressure. This scenario has been discussed theoretically [2,3] and experimentally [4–6]. Based on the idea that the magnetism is strongly coupled with the crystal structure, a recent paper has pointed out that even a partial spin disorder in the α phase can result in a decrease in the energy of lattice fluctuations required for transition to the ϵ phase [3]. It has also been predicted that intermediate structures with complicated magnetic structures such as spin spirals can lower the barrier between the α and ϵ phases [2]. Using x-ray absorption spectroscopy and x-ray magnetic circular dichroism (XMCD), Mathon *et al.* have reported that the magnetic collapse precedes the structural phase transition [5]. This is because the XMCD signal significantly decreases before the transition to the ϵ phase, which is regarded as an experimental signature of this scenario. In the case of iron nanoparticles, the precedence is reported to be more pronounced [6].

The second scenario is the transition driven by shear stress or shuffle motion. Although hydrostatic pressure conditions cannot produce shear, a shuffle-only mode [$T_1(N)$ mode in α phase] is theoretically allowed to reach the barrier below 30 GPa [7]. It has also been suggested that shear stress is required to initiate the α-ϵ transition, and the transition appears at larger volumes and lower applied pressure with increasing shear [8,9]. The importance of shear is consistent with the experimental observations that the onset and the pressure range of the transition strongly depend on nonhydrostaticity of the material used for the pressure-transmitting medium [10]. In contrast to the first scenario, the collapse of the ferromagnetic order in the ϵ phase is attributed to change in the structural symmetry, i.e., the spontaneous shear strains

*naoki@sci.hiroshima-u.ac.jp

and the shuffle motion involved in the Burgers reconstructive transition mechanism lead to the disappearance of the ferromagnetic order [11].

In this paper, the two controversial scenarios are experimentally examined by combined measurements of XMCD and extended x-ray absorption fine structure (EXAFS). The combined measurement is a very suitable method to investigate the relationship between the α-ϵ and magnetic transition pathways, because EXAFS and XMCD probe the local crystal structure and magnetism of the same irradiated area, respectively. In this study, we have measured the EXAFS and XMCD spectra at the Fe K edge under quasihydrostatic pressures using a helium pressure-transmitting medium. Helium provides the most suitable pressure condition to minimize the shear stress because helium remains soft and nearly hydrostatic even after its solidification at 11.5 GPa [12]. We note that an excellent EXAFS study in this regard has been already performed by Wang and Ingalls [13], and they observed structural anomalies at the transition of iron, such as a distorted ϵ phase with a large c/a ratio and expanded lattice constant in the α phase. We verify that these anomalies remain stable under quasihydrostatic pressures because previous EXAFS study was not performed under hydrostatic conditions [13]. In this study, sharp changes in both EXAFS and XMCD spectra are observed simultaneously at the onset of the transition, indicating that the precedence of the magnetic transition over the structural one does not occur. Furthermore, a model with an orthorhombic crystal structure is tested to fit the EXAFS profiles in order to demonstrate how shear and shuffle motions progress at the martensitic α-ϵ transition. We conclude that shear stress is important to initiate the α-ϵ transition.

II. EXPERIMENTAL AND THE EXAFS FITTING PROCEDURES

The EXAFS and XMCD measurements at the Fe K edge were performed on beamline 39XU at SPring-8 [14]. XMCD spectra were measured by the helicity modulation technique using circularly polarized beam from a diamond $\lambda/4$ wave plate. The EXAFS spectra were measured after removing the $\lambda/4$ wave plate from the x-ray path, so that incident x ray was horizontally polarized for the EXAFS measurements. We repeated this sequence at all pressures measured in this study. The incident x-ray beam was focused by Kirkpatrick and Baez mirrors and set to a size of 9(h)×2(v) μm^2 at the sample position. Diamond anvil cells were used for applying pressure. We used nanopolycrystalline diamond (NPD) anvils to remove Bragg diffraction from the anvil, which frequently appears during the EXAFS measurements [15,16]. A polycrystalline iron foil 4 μm in thickness was placed inside a Re gasket hole. We measured the pressure dependence of the EXAFS and XMCD spectra again after loading a new iron foil to confirm reproducibility. All measurements were done at room temperature. A magnetic field H of 0.6 T was applied parallel to the incident x-ray beam and in the direction of the surface normal of the sample foil. The conventional ruby fluorescence method was used for pressure calibration.

The software packages, ATHENA and ARTEMIS using the IFEFFIT library were used for the analysis of EXAFS [17]. The theoretical standards were outputted by the built-in FEFF code (FEFF6 [18]), and the local structure around the iron atom was determined from curve fitting in the radial space. The normalized EXAFS profile $\chi(k)$ to model the experimental data is represented by a sum over jth path as [19]

$$\chi(k) = \sum_j \frac{S_0^2 N_j f_i(k)}{k R_j^2} \sin(2kR_j + \phi_j(k)) e^{-2k^2\sigma_j^2 - 2R_j/\lambda(k)}, \tag{1}$$

where R_j is the distance from the central absorbing atom to the jth shell, N_j is the coordination number, $f_j(k)$ is the complex backscattering amplitude, ϕ_j is the phase shift, σ_j is the Debye-Waller factor (DWF), $\lambda(k)$ is the mean free path of the photoelectron, and S_0 is the overall amplitude reduction factor due to many-body effects. The wave number k is defined as $k = \sqrt{\frac{2m}{\hbar^2}(E - E_0)}$, where m is the mass of electron, E is the incident photon energy, E_0 is the photon energy at the absorption edge, $\hbar$ is the Plank constant divided by 2π. The higher cumulants C_{3j} and C_{4j} were not taken into account in this study. The k range used for Fourier transformation was 2.0–13.3 Å^{-1}, and the curve-fitting R range was set to 1.2–6.0 Å. The correlated Debye model was used to calculate the DWF for each scattering path [20]. The use of the correlated Debye model followed the procedure from prior EXAFS work of iron [13]. The Debye temperature (θ_D) was determined separately for the ϵ and α phases.

The actual distance to the jth shell from the central absorbing atom, R_j, is expressed as

$$R_j = R_j^{\text{eff}} + \Delta R_j, \tag{2}$$

where R_j^{eff} is the calculated atomic distance of the initial crystal structure and ΔR_j is a fitting parameter that represents deviation from the calculated R_j^{eff}. In conventional EXAFS analysis, a large number of ΔR_j are separately optimized unless taking the symmetry of the crystal structure into account. To avoid this problem, we reduced the number of ΔR_j by imposing constraints based on the crystal structure. The constraints ensure invariance of the symmetry of the crystal structure after fit. Details about the fitting procedure are described in Appendix.

A constant value was used for θ_D of the α phase, and only θ_D of the ϵ phase was optimized at the pressures above the transition. This is because θ_D of the α phase is easy to diverge when the α phase has small abundance. The averaged value of θ_D before the transition was used for the constant value of θ_D for the α phase. Since the calculated value of S_0^2 for ϵ phase was similar to that for α phase, the α phase abundance, w_α, was estimated from the fit using the linear combination of the EXAFS functions of α phase [$\chi^\alpha(k)$] and ϵ phase [$\chi^\epsilon(k)$] as $\chi(k) = w_\alpha \chi^\alpha(k) + (1 - w_\alpha)\chi^\epsilon(k)$.

III. RESULTS AND DISCUSSION

A. Comparison between the magnetic and structural transitions

Figure 1 shows XMCD and x-ray absorption near edge structure (XANES) spectra at selected pressures. Subtle changes due to the compression are observed in the XMCD and XANES profiles at pressures below the transition up to 14.6 GPa. The XMCD amplitude abruptly decreases at 14.9

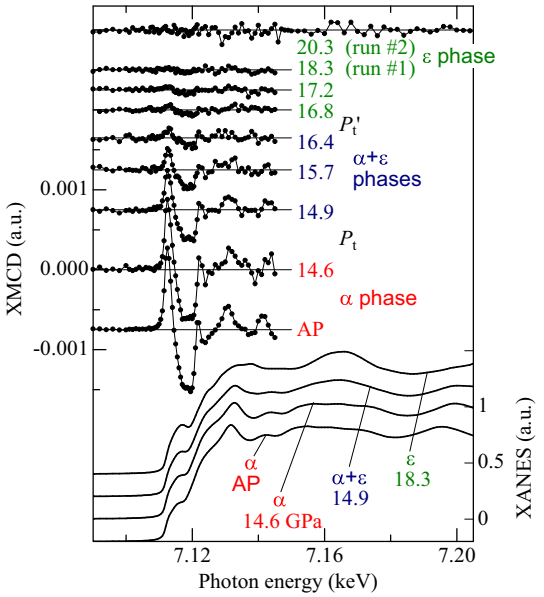

FIG. 1. (Color online) XMCD (top) and x-ray absorption (XANES: bottom) spectra of iron at the Fe K edge under selected pressures. Each spectrum is shifted upward for clarity.

GPa together with the modification of the XANES spectra. Thus the pressure corresponding to the onset of the structural and magnetic transition is defined as $P_t \approx 14.8$ GPa. With further applied pressure, the XMCD amplitude gradually decreases and becomes very small ($\leqslant 8\times10^{-5}$) above $P_t' \approx$ 16.6 GPa. The XMCD spectrum of the second run vanishes within the noise level at 20.3 GPa. The spectral change in the XANES profile indicates that most part of the iron transforms into the ϵ phase at P_t'.

The collapse of the ferromagnetic order is demonstrated in Fig. 2, wherein the integrated intensity of XMCD (I_{XMCD}) is plotted as a function of pressure. I_{XMCD} is evaluated from the integration of the absolute value of the XMCD spectrum in the energy range 7109–7121.5 eV. The integrated intensity of XMCD at the Fe K edge can be used to monitor the variation in

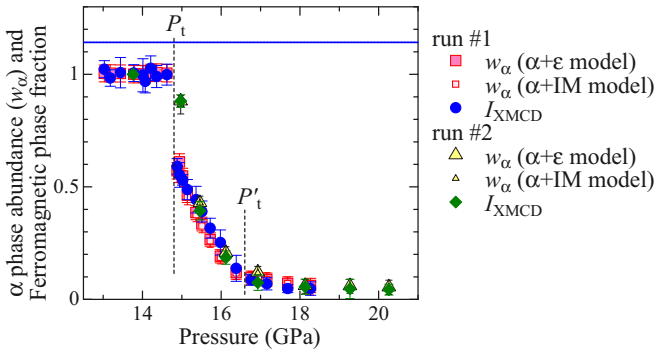

FIG. 2. (Color online) Pressure dependence of normalized ferromagnetic phase fraction and relative α phase abundance (w_α) evaluated from the XMCD and EXAFS spectra, respectively. For comparison, the ferromagnetic phase fraction is normalized by the average value of I_{XMCD} in the range between 13 GPa and P_t. The (blue) horizontal line indicates the normalized magnitude of I_{XMCD} at AP.

the net magnetic moment with pressure through modifications of the $4p$ band induced by changes in the $3d$ moment [5,21]. In this study, we assume that I_{XMCD} is proportional to the magnetization; I_{XMCD} becomes zero when the magnetic state of the sample is nonmagnetic or antiferromagnetic. The evaluated I_{XMCD} appears constant in the range 13 GPa $\leqslant P \leqslant P_t$, and its magnitude is 0.87 times smaller than that at ambient pressure (AP). The small suppression of I_{XMCD} implies that the magnetization of the α phase is quite stable against the pressure-induced volume compression. A striking feature of the first run is the sharp drop of the normalized I_{XMCD} to ≈ 0.6 at P_t and the subsequent steep slope of I_{XMCD} up to P_t'. Above P_t', the slope becomes moderate and I_{XMCD} approaches zero. The second run reproduces the entire pressure variation of the first run. A small drop of the normalized I_{XMCD} to $\approx$0.9 is observed just above P_t in the case of the second run.

To investigate the coincidence of the structural transition and the magnetic collapse, the α phase abundance (w_α) is estimated from the EXAFS spectra. The EXAFS spectra are fitted by a model assuming the coexistence of the α and ϵ phases ($\alpha + \epsilon$ model). As shown in Fig. 2, w_α well traces the pressure dependence of I_{XMCD} within small experimental errors. The coincidence is also observed for the $\alpha +$ IM model that is a model discussed later. Therefore the onsets of the structural and magnetic transitions occur simultaneously. This coincidence is interpreted as that the ϵ phase has no ferromagnetic order, whereas the ferromagnetic order in α phase maintains comparable magnitude with that at AP even during the transition. Because w_α is as large as the magnitude of the normalized I_{XMCD}, the moderate slope above P_t' represents that the residual α phase is responsible for the weak ferromagnetic component in the sample above P_t'; both the ferromagnetic component and residual α phase gradually decrease with increasing pressure. This is convincing evidence that the ϵ phase is nonmagnetic or antiferromagnetic. In contrast to the scenario of magnetic driven transition, we conclude that the ferromagnetism instability does not occur in the α phase; the ferromagnetic α phase undergoes direct transition to the nonmagnetic or antiferromagnetic ϵ phase. Furthermore, the low-spin state with an intermediate magnetic moment of about $1\mu_B$, which is reported and discussed in Ref. [5], is probably absent.

B. EXAFS analysis: $\alpha + \epsilon$ model

The results of EXAFS analysis using the $\alpha + \epsilon$ model are summarized in Figs. 3 and 4. The obtained EXAFS $\chi(k)k^2$ oscillation [Fig. 3(a)] is glitch-free up to $k = 15$ Å^{-1}, which is an advantage of utilizing the NPD anvils [15]. The $\chi(k)k^2$ oscillation is modified due to the α-ϵ transition. In the $\alpha + \epsilon$ model, the relation $\sqrt{2}a_\alpha = c_\epsilon$ is assumed as a constraint on the lattice constants of the α and ϵ phases. The constraint is employed as a result of previous XRD experiments [22,23]; the 0002 Bragg reflection from ϵ phase appears at the same Bragg angle of the 110 reflection from α phase, indicating that the d spacing of the atomic plane $(110)_\alpha$ is similar to that of the conjugate $(0002)_\epsilon$ atomic plane after the shuffle motion of the transition. Using the constraint, the fitting parameters are optimized to minimize the R factor for the magnitude of Fourier transforms of $\chi(k)k^2$ to a value less than 8×10^{-4}

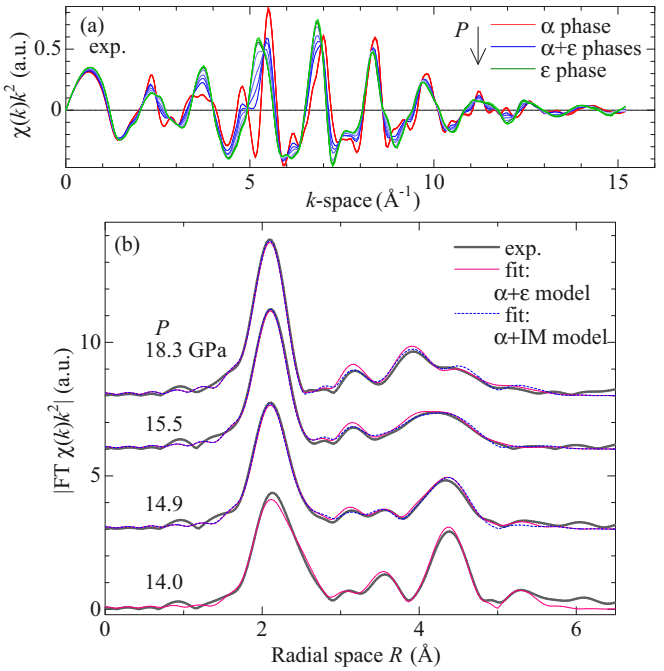

FIG. 3. (Color online) (a) The $\chi(k)k^2$ profile obtained from the first run. (b) Magnitude of the Fourier transforms of the $\chi(k)k^2$ (thick solid lines), the fitted curves of the $\alpha + \epsilon$ model (thin solid lines), and the curves of the $\alpha +$ IM model (thin broken lines) at selected pressures.

[Fig. 3(b)]. As shown in Fig. 4, the lattice constants a_α and c_ϵ decrease monotonically with increasing pressure, whereas a_ϵ increases up to ∼16 GPa and decreases at higher pressures. The small a_ϵ value near P_t results in a large c_ϵ/a_ϵ ratio of the range 1.61–1.62; the ratio eventually reduced to a constant value of about 1.596 with increasing pressure. The large c_ϵ/a_ϵ at the onset of transition is due to the minimal a_ϵ value of the second run, for which the ϵ phase abundance is only 10%. The

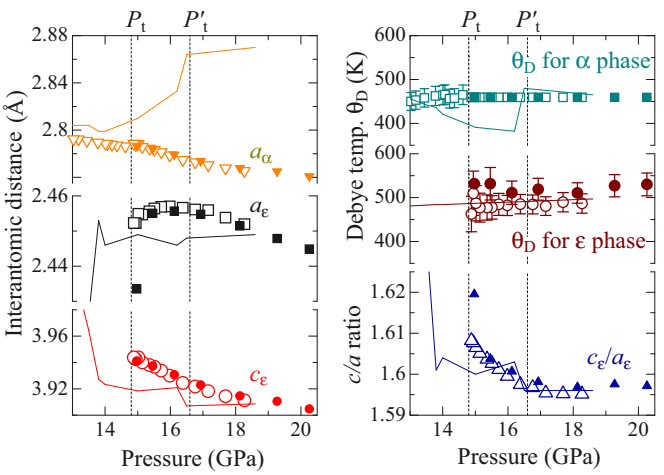

FIG. 4. (Color online) Fitted results of lattice constants and c/a ratio obtained using the $\alpha + \epsilon$ model. Open and closed symbols correspond to the results from the first and second runs, respectively. The thin solid lines indicate the data taken from Ref. [13] for comparison.

bond length of α phase, which is typically $\frac{\sqrt{3}}{2}a_\alpha = 2.42$ Å at P_t, is close to the minimal a_ϵ value. This implies that influence from the interface between α and ϵ phases is pronounced when the ϵ phase in the minor abundance at the onset.

As shown in Fig. 4, the fitting results are qualitatively consistent with the previous EXAFS results by Wang and Ingalls [13]; however, the anomalously expanded a_α does not appear near the offset P_t' of our model. This inconsistency is attributed to the fact that compression of c_ϵ counteracts the expansion of a_α via the strong constraint $\sqrt{2}a_\alpha = c_\epsilon$, since the α phase abundance is less than 10% at P_t'. It is considered that the α phase with anomalously expanded a_α is one of possible structures when the α phase has small abundance at the offset. This is because the influence of the majority phase on the crystal structure of the minority phase occurs near the interface at both onset and offset; the large a_ϵ of the ϵ phase is expected to expand a_α at the interface of the offset. We note that our model reproduces the expansion of a_α at P_t' if the constraint $\sqrt{2}a_\alpha = c_\epsilon$ is off. The fit with $\sqrt{2}a_\alpha \neq c_\epsilon$ model, however, failed to reproduce other structural parameters, e.g., this model yields a value of $c_\epsilon/a_\epsilon \approx 1.575$ at the onset, which is too small a value for the initial structure of the ϵ phase.

C. EXAFS analysis: $\alpha +$ IM model

We next examine a model assuming the coexistence of the α phase and an orthorhombic intermediate (IM) structure instead of the ϵ phase ($\alpha +$ IM model). This is a model in order to investigate how shear and shuffle motions proceed during the transition. The orthorhombic unit cell (space group: $Cmcm$), which has lower symmetry than the bcc and hcp structures, enables us to introduce arbitrary displacements from the atomic position for the α phase to that for the ϵ phase (see Fig. 6). Iron atoms in the IM phase occupy $4c$ site at $(0, y, \frac{1}{4})$. The length of the shortest Fe-Fe bond in the $(001)_{IM}$ plane is represented by l_b. The lattice constants and y components of the atomic position are set to $a_\alpha = a_{IM} = \frac{1}{\sqrt{2}}c_{IM} = \frac{1}{\sqrt{2}}b_{IM}$ and $y = \frac{1}{4}$ for the α phase, and $a_\epsilon = a_{IM} = \frac{1}{\sqrt{3}}b_{IM}$, $c_\epsilon = c_{IM}$, and $y = \frac{1}{3}$ for the ϵ phase. The angle θ_b between adjacent bonds with length l_b is 70.5° and 60° for the α and ϵ phases, respectively. Using the fitted values of a_{IM} and b_{IM}, l_b and θ_b are evaluated from the following equations: $l_b = \sqrt{a_{IM}^2 + b_{IM}^2}/2$ and $\theta_b = 2\arctan(a_{IM}/b_{IM})$. The shuffle and shear motions are expressed by the two order parameters y and θ_b, respectively. The atomic position y corresponds to antiparallel shifting of the atoms due to the shuffle motion between the adjacent $(001)_{IM}$ planes. The angle θ_b is associated with shear motion in the $(001)_{IM}$ plane. In this model, a degenerated single scattering EXAFS path for the ϵ phase is divided into two or three different paths for the IM phase. The detailed procedure of fitting is described in Appendix.

The fitted profile of this model and the determined structural parameters are shown in Figs. 3(b) and 5, respectively. The $\alpha +$ IM model gives better fitted profiles than the $\alpha+\epsilon$ model. The pressure dependencies of l_b and c_{IM}/l_b are similar to those of the $\alpha + \epsilon$ model. The bond length l_b, which is approximately equivalent to a_ϵ, increases in the pressure range from P_t to ∼16 GPa and decreases at higher pressures. The values of y and θ_b are close to the ideal values of the ϵ phase even at the

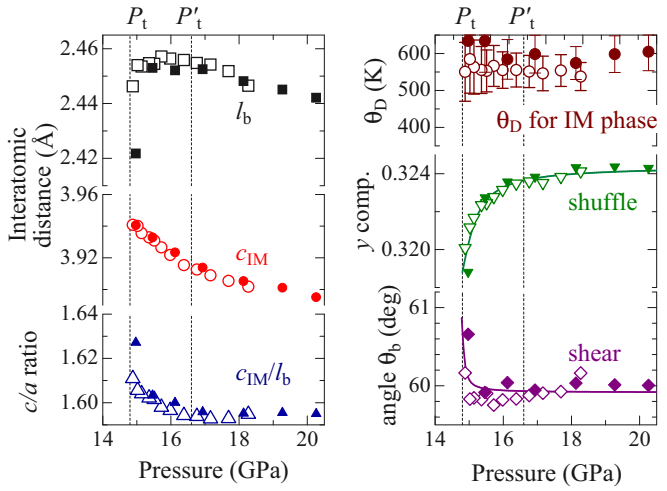

FIG. 5. (Color online) Fitting results of the $\alpha + \mathrm{IM}$ model. Open and closed symbols correspond to the data of first and second runs, respectively. Solid lines are guides to the eye.

onset, implying that the martensitic phase appears initially as a slightly distorted ϵ phase. A notable result of this model is that the curves of y and θ_b versus pressure appear dissimilar. A closer look at the data reveals that θ_b decreases from 70.5° to 60° immediately after the transition together with a slight deviation ($\theta_b = 60.7°$) near P_t, whereas the y component gradually increases after the jump from $\frac{1}{4}$ to 0.319 at P_t. Above P'_t, y reaches a constant value of 0.324 that is still smaller than the ideal value for the ϵ phase, $y = \frac{1}{3}$. This result indicates that shear motion is completed after the appearance of the martensitic phase by more than 50%, while the shuffle motion is unfinished and continuously progresses during the transition. Structural distortion due to the incompleteness of the shuffle movement is gradually released with increasing martensitic phase; however, a small distortion remains above P'_t.

The structural transformation determined from the $\alpha + \mathrm{IM}$ model is illustrated in Fig. 6. The sudden completion of the shear movement can attributed to the Burgers-type transformation [24], wherein the conjugate atomic planes are set to $(112)_\alpha \parallel (1100)_\epsilon$ and $(1\bar{1}0)_\alpha \parallel (0002)_\epsilon$. As shown in the middle panel of Fig. 6, the Burgers-type model allows completion of shear movement along $[11\bar{1}]_\alpha$ direction in the $(112)_\alpha$ plane unless changing l_b, so that it is easy to match the crystal structures of the martensitic and parent phases at the interface. Thus the small l_b value near P_t against the sudden decrease in θ_b is elucidated by the Burgers-type model. The Burgers-type transformation is a plausible model compared with another model [13,22,25], in which the conjugate atomic planes are set to $(002)_\alpha \parallel (\bar{2}110)_\epsilon$ and $(1\bar{1}0)_\alpha \parallel (0002)_\epsilon$ [26]. Hypothesizing the latter model, l_b should increase simultaneously with the progress of the shear movement, which is inconsistent with the present results of l_b and θ_b. We note that the Burgers-type model is also discussed as a probable transition model of iron in Ref. [13].

The precedence of the shear movement over shuffle motion experimentally demonstrates that the shear stress is required to initiate the α-ϵ transition. The shear stress leads to the rapid shear movement, and it works as the trigger of the α-ϵ

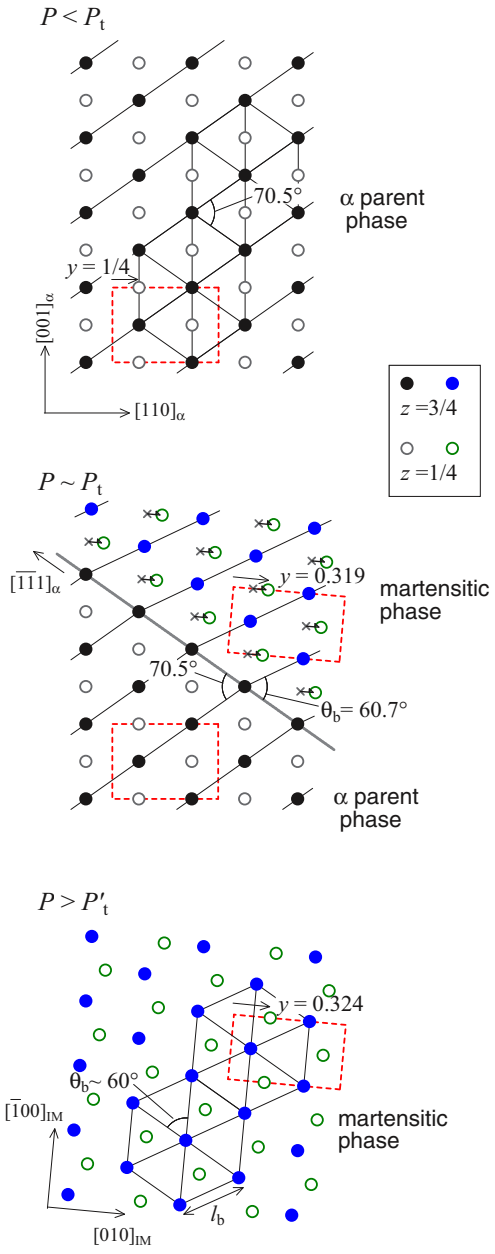

FIG. 6. (Color online) Schematic of the martensitic transition of iron based on the Burgers model. The atomic arrangements are viewed from the $[001]_{IM}$ direction [24]. The broken-line rectangles depict unit cells of the orthorhombic lattice (space group $Cmcm$) for each phase. The small arrows in the martensitic phase indicate displacements related to the y parameter due to shuffle motion. These figures are depicted on the basis of the configuration that l_b is unchanged by the shear motion.

transition. The importance of the shear stress for the transition is consistent with the discussion in the second scenario by Caspersen *et al.* [8,9]. They have theoretically predicted that hydrostatic conditions do not provoke the transition, whereas the transition appears at lower applied pressure with increasing shear stress. In our experimental condition, shear stress is provided under the quasihydrostatic conditions after the solidification of helium above 11.5 GPa. The generated shear stresses of the solid helium are probably small but

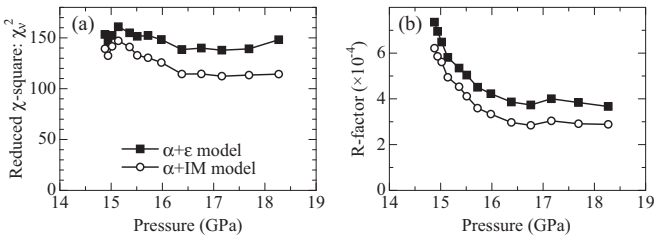

FIG. 7. Comparison of (a) reduced χ-square (χ_ν^2) and (b) R factor between $\alpha + \epsilon$ model (closed squares) and $\alpha +$ IM model (open circles). All data are taken from the first run.

adequate to initiate the martensitic phase at P_t. This result also indicates that the shear and shuffle motions are decoupled. The gradual progress of the shuffle motion is attributed to (i) the enhanced effect of the interface at the onset and/or (ii) successive shuffle motion of the $(001)_{IM}$ layers. As mentioned above, it is preferable to match the crystal structure between the parent and martensitic phases at the interface when one of the two phases is in very minor abundance. In this case, the shuffle motion near the interface does not occur to match the crystal structure at the interface; consequently, structural distortion due to the incomplete shuffle yields a y value smaller than $\frac{1}{3}$. The distortion near the interface is gradually released as the abundance of the martensitic phase increases with increasing pressure. The phenomenon of successive shuffle motion has been proposed in a recent theoretical paper [27]. In comparison with the simultaneous shuffle motion, successive shuffle follows an energetically lower transition pathway. The theoretical study has reported that the successive shuffle transformation nucleates from one single shuffle event, which is possibly initiated by initial shear. In the case of the successive shuffle model, we speculate that the nucleation first appears far from the interface, and then the successive shuffle motion propagates towards the interface.

The fitted profiles of the $\alpha +$ IM model reproduce the experimental profiles with the reduced χ-square (χ_ν^2) and R-factor values being smaller by a factor of 0.8–0.9 than those of the $\alpha + \epsilon$ model (Fig. 7). The χ_ν^2 is a good tool for comparing the two models for the fits to the same data [28]. The smaller χ_ν^2 values of the $\alpha +$ IM model statistically support that this model is a more probable model than the $\alpha + \epsilon$ model. Therefore it is inferred that the martensitic phase maintains a structure with lower symmetry than the hcp structure even above P_t' since the maximal y value slightly deviates from $\frac{1}{3}$. A symmetry lower than that of the hcp structure may be a possible crystal structure if the high-pressure phase of iron is antiferromagnetic or possesses a more complicated magnetic structure. A number of studies have been proposed the existence of magnetic structures such as antiferromagnetic order [29,30] and noncollinear magnetic structure [31–33]. We also note the observation of two Raman bands at moderate pressures between 15 and 40 GPa; one is identified as the E_{2g} fundamental mode of the hcp lattice, whereas the other is a forbidden band for the nonmagnetic hcp lattice of iron [29,34]. However, the actual magnetic structure has not thus far been experimentally determined. More detailed studies are required to investigate the relationship between the structure and magnetism of the high-pressure phase of iron.

IV. CONCLUSION

In conclusion, the α-ϵ transition pathway of iron was investigated using EXAFS and XMCD spectra at the Fe K edge under quasihydrostatic pressures. This study revealed that shear stress is required to initiate the transition. The transition is not a magnetism-driven transition because the ferromagnetism in the α phase remains stable at P_t, and the α-ϵ structural transition simultaneously occurs with the collapse of ferromagnetism in the ϵ phase. The transition pathway consists of two steps: sudden appearance of the nonmagnetic (or antiferromagnetic) distorted ϵ phase due to the shear stress and the subsequent gradual disappearance of the residual ferromagnetic α phase. The distortion in the ϵ phase is attributed to the unfinished shuffle motion, and slight distortion remains even above P_t'.

ACKNOWLEDGMENTS

We would like to thank H. Tanaka, K. Fujii, and C. Temba for their technical support. The EXAFS and XMCD measurements were performed at SPring-8 with the approval of PRC-JASRI (Nos. 2012A1380, 2013A1460, and 2013B1284).

APPENDIX: FITTING MODELS FOR THE EXAFS ANALYSIS

1. $\alpha + \epsilon$ model

Coexistence of $\alpha + \epsilon$ phases was assumed at the transition region above P_t in this model. We imposed constraints on ΔR_j to ensure the symmetry of hcp structure after fit. For this purpose, R_j^{eff} and ΔR_j for jth path were rewritten as a function of lattice constants of the hcp structure and their deviations, i.e., a_ϵ, c_ϵ, Δa_ϵ, and Δc_ϵ. Only the first-order terms of Δa_ϵ and Δc_ϵ were used to formulate ΔR_j, and all higher-order terms were neglected. R_j and ΔR_j for the jth single scattering (SS) paths are listed in Table I. All distances and their deviation for

TABLE I. EXAFS parameters related to the crystal structure of ϵ phase in the $\alpha + \epsilon$ model. Parameters for jth single scattering (SS) paths of $R_j^{\text{eff}} \leqslant 6$ Å are tabulated. R_j^{eff} is calculated using the default values $a_\epsilon = 2.456$ Å and $c_\epsilon = 3.943$ Å.

j	N_j	R_j^{eff} (Å)	description of R_j^{eff}	description of ΔR_j
1	6	2.429	$\sqrt{\left(\frac{\sqrt{3}a_\epsilon}{3}\right)^2 + \left(\frac{c_\epsilon}{2}\right)^2}$	$\left(\frac{a_\epsilon \Delta a_\epsilon}{3} + \frac{c_\epsilon \Delta c_\epsilon}{4}\right)/R_1^{\text{eff}}$
2	6	2.456	a_ϵ	$a_\epsilon \Delta a_\epsilon / R_2^{\text{eff}}$
3	6	3.454	$\sqrt{\left(\frac{2\sqrt{3}a_\epsilon}{3}\right)^2 + \left(\frac{c_\epsilon}{2}\right)^2}$	$\left(\frac{4a_\epsilon \Delta a_\epsilon}{3} + \frac{c_\epsilon \Delta c_\epsilon}{4}\right)/R_3^{\text{eff}}$
4	2	3.943	c_ϵ	$c_\epsilon \Delta c_\epsilon / R_4^{\text{eff}}$
5	12	4.238	$\sqrt{\left(\frac{\sqrt{21}a_\epsilon}{3}\right)^2 + \left(\frac{c_\epsilon}{2}\right)^2}$	$\left(\frac{7a_\epsilon \Delta a_\epsilon}{3} + \frac{c_\epsilon \Delta c_\epsilon}{4}\right)/R_5^{\text{eff}}$
6	6	4.254	$\sqrt{3}a_\epsilon$	$3a \Delta a_\epsilon / R_6^{\text{eff}}$
7	12	4.645	$\sqrt{a_\epsilon^2 + c_\epsilon^2}$	$(a_\epsilon \Delta a_\epsilon + c_\epsilon \Delta c_\epsilon)/R_7^{\text{eff}}$
8	6	4.912	$2a_\epsilon$	$4a_\epsilon \Delta a_\epsilon / R_8^{\text{eff}}$
9	12	5.479	$\sqrt{\left(\sqrt{\frac{13}{3}}a_\epsilon\right)^2 + \left(\frac{c_\epsilon}{2}\right)^2}$	$\left(\frac{13a_\epsilon \Delta a_\epsilon}{3} + \frac{c_\epsilon \Delta c_\epsilon}{4}\right)/R_9^{\text{eff}}$
10	12	5.800	$\sqrt{(\sqrt{3}a_\epsilon)^2 + c_\epsilon^2}$	$(3a_\epsilon \Delta a_\epsilon + c_\epsilon \Delta c_\epsilon)/R_{10}^{\text{eff}}$

TABLE II. The j-i path length and their deviation for the orthorhombic IM phase used in the α + IM model. $R^{\rm eff}_{j\text{-}i}$ is calculated using the default values $a_{\rm IM} = \frac{1}{\sqrt{3}} b_{\rm IM} = 2.456$ Å, $c_{\rm IM} = 3.943$ Å, and $y = \frac{1}{3}$. Note that the subscripts "IM" of the lattice constants ($a_{\rm IM}$, $b_{\rm IM}$, and $c_{\rm IM}$) are not shown here for simplicity.

j-i	$N_{j\text{-}i}$	$R^{\rm eff}_{j\text{-}i}$ (Å)	description of $R^{\rm eff}_{j\text{-}i}$	description of $\Delta R_{j\text{-}i}$
1-1	4	2.429	$\sqrt{\left(\frac{a}{2}\right)^2 + \left[\left(\frac{1}{2} - 2y\right)b\right]^2 + \left(\frac{c}{2}\right)^2}$	$\left\{\frac{a\Delta a}{4} + b\left(\frac{1}{2} - 2y\right)\left[\Delta b\left(\frac{1}{2} - 2y\right) - 2b\Delta y\right] + \frac{c\Delta c}{4}\right\} / R^{\rm eff}_{1\text{-}1}$
1-2	2	2.429	$\sqrt{[(1-2y)b]^2 + \left(\frac{c}{2}\right)^2}$	$\left\{b(1-2y)[\Delta b(1-2y) - 2b\Delta y] + \frac{c\Delta c}{4}\right\} / R^{\rm eff}_{1\text{-}2}$
2-1	4	2.456	$\sqrt{\left(\frac{a}{2}\right)^2 + \left(\frac{b}{2}\right)^2}$	$\left(\frac{a\Delta a}{4} + \frac{b\Delta b}{4}\right) / R^{\rm eff}_{2\text{-}1}$
2-2	2	2.456	a	$a\Delta a / R^{\rm eff}_{2\text{-}2}$
3-1	2	3.454	$\sqrt{(2yb)^2 + \left(\frac{c}{2}\right)^2}$	$\left[2yb(2y\Delta b + 2b\Delta y) + \frac{c\Delta c}{4}\right] / R^{\rm eff}_{3\text{-}1}$
3-2	4	3.454	$\sqrt{a^2 + [(1-2y)b]^2 + \left(\frac{c}{2}\right)^2}$	$\left\{a\Delta a + b(1-2y)\left[\Delta b(1-2y) - 2b\Delta y\right] + \frac{c\Delta c}{4}\right\} / R^{\rm eff}_{3\text{-}2}$
4	2	3.943	c	$c\Delta c / R^{\rm eff}_{4}$
5-1	4	4.238	$\sqrt{a^2 + (2yb)^2 + (\frac{c}{2})^2}$	$\left[a\Delta a + 2yb(2y\Delta b + 2b\Delta y) + \frac{c\Delta c}{4}\right] / R^{\rm eff}_{5\text{-}1}$
5-2	4	4.238	$\sqrt{\left(\frac{3a}{2}\right)^2 + \left[\left(\frac{1}{2} - 2y\right)b\right]^2 + \left(\frac{c}{2}\right)^2}$	$\left\{\frac{9a\Delta a}{4} + b\left(\frac{1}{2} - 2y\right)\left[\Delta b\left(\frac{1}{2} - 2y\right) - 2b\Delta y\right] + \frac{c\Delta c}{4}\right\} / R^{\rm eff}_{5\text{-}2}$
5-3	4	4.238	$\sqrt{\left(\frac{a}{2}\right)^2 + \left[\left(\frac{3}{2} - 2y\right)b\right]^2 + \left(\frac{c}{2}\right)^2}$	$\left\{\frac{a\Delta a}{4} + b\left(\frac{3}{2} - 2y\right)\left[\Delta b\left(\frac{3}{2} - 2y\right) - 2b\Delta y\right] + \frac{c\Delta c}{4}\right\} / R^{\rm eff}_{5\text{-}3}$
6-1	2	4.254	b	$b\Delta b / R^{\rm eff}_{6\text{-}1}$
6-2	4	4.254	$\sqrt{\left(\frac{3a}{2}\right)^2 + \left(\frac{b}{2}\right)^2}$	$\left(\frac{9a\Delta a}{4} + \frac{b\Delta b}{4}\right) / R^{\rm eff}_{6\text{-}2}$
7-1	8	4.645	$\sqrt{\left(\frac{a}{2}\right)^2 + \left(\frac{b}{2}\right)^2 + c^2}$	$\left(\frac{a\Delta a}{4} + \frac{b\Delta b}{4} + c\Delta c\right) / R^{\rm eff}_{7\text{-}1}$
7-2	4	4.645	$\sqrt{a^2 + c^2}$	$(a\Delta a + c\Delta c) / R^{\rm eff}_{7\text{-}2}$
8-1	4	4.912	$\sqrt{a^2 + b^2}$	$(a\Delta a + b\Delta b) / R^{\rm eff}_{8\text{-}1}$
8-2	2	4.912	$2a$	$4a\Delta a / R^{\rm eff}_{8\text{-}2}$
9-1	4	5.479	$\sqrt{(2a)^2 + [(1-2y)b]^2 + \left(\frac{c}{2}\right)^2}$	$\left\{4a\Delta a + b(1-2y)\left[\Delta b(1-2y) - 2b\Delta y\right] + \frac{c\Delta c}{4}\right\} / R^{\rm eff}_{9\text{-}1}$
9-2	4	5.479	$\sqrt{\left(\frac{3a}{2}\right)^2 + \left[\left(\frac{3}{2} - 2y\right)b\right]^2 + \left(\frac{c}{2}\right)^2}$	$\left\{\frac{9a\Delta a}{4} + b\left(\frac{3}{2} - 2y\right)\left[\Delta b\left(\frac{3}{2} - 2y\right) - 2b\Delta y\right] + \frac{c\Delta c}{4}\right\} / R^{\rm eff}_{9\text{-}2}$
9-3	4	5.479	$\sqrt{\left(\frac{a}{2}\right)^2 + \left[\left(\frac{1}{2} + 2y\right)b\right]^2 + \left(\frac{c}{2}\right)^2}$	$\left\{\frac{a\Delta a}{4} + b\left(\frac{1}{2} + 2y\right)\left[\Delta b\left(\frac{1}{2} + 2y\right) + 2b\Delta y\right] + \frac{c\Delta c}{4}\right\} / R^{\rm eff}_{9\text{-}3}$
10-1	4	5.800	$\sqrt{b^2 + c^2}$	$(b\Delta b + c\Delta c) / R^{\rm eff}_{10\text{-}1}$
10-2	8	5.800	$\sqrt{\left(\frac{3a}{2}\right)^2 + \left(\frac{b}{2}\right)^2 + c^2}$	$\left(\frac{9a\Delta a}{4} + \frac{b\Delta b}{4} + c\Delta c\right) / R^{\rm eff}_{10\text{-}2}$

the multiple scatting (MS) paths were constructed by a linear combination of those of the SS paths. For the α phase, ΔR_j for jth path is set to be $\Delta R_j = A R^{\rm eff}_j$, where A is a fitting parameter as a proportional constant to ensure the symmetry of bcc structure. Because R_j and E_0 are highly correlated, only R_j was treated as a "guess" parameter, whereas E_0 was treated as a "set" parameter in the pressure range around the transition ($P \geqslant P_{\rm t}$). The average of the optimized values in the pressure range outside the transition was used for the "set" value of E_0.

2. α + IM model

Coexistence of α phase and IM phase was assumed at the transition above $P_{\rm t}$ in this model. Orthorhombic unit cell (space grou: $Cmcm$) was considered as an IM phase to introduce arbitrary displacement of the atomic position between α phase and ϵ phase. Because the orthorhombic unit cell is regarded as a structure with a symmetry lower than that of ϵ phase (also of α phase), a degenerated jth scattering path for the ϵ phase is divided into two or three ($i = 1,2$ or $i = 1,2,3$) different scattering paths. Each path distance $R^{\rm eff}_{j\text{-}i}$ and its deviation $\Delta R_{j\text{-}i}$ were rewritten as a function of $a_{\rm IM}$, $b_{\rm IM}$, $c_{\rm IM}$, y, and their deviations. The path distance for j-ith path ($R^{\rm eff}_{j\text{-}i}$) and the deviation ($\Delta R^{\rm eff}_{j\text{-}i}$) are tabulated in Table II. This conversion was applied to all SS paths and the collinear MS paths. Path distances and their deviation for the noncollinear MS paths remained similar to those for the $\alpha + \epsilon$ model because of the relatively weak contribution to the result of fit.

[1] D. Bancroft, E. L. Peterson, and S. Minshall, J. Appl. Phys. **27**, 291 (1956).

[2] M. Ekman, B. Sadigh, K. Einarsdotter, and P. Blaha, Phys. Rev. B **58**, 5296 (1998).

[3] S. Mankovsky, S. Polesya, H. Ebert, W. Bensch, O. Mathon, S. Pascarelli, and J. Minár, Phys. Rev. B **88**, 184108 (2013).

[4] S. Klotz and M. Braden, Phys. Rev. Lett. **85**, 3209 (2000).

[5] O. Mathon, F. Baudelet, J. P. Itié, A. Polian, M. d'Astuto, J. C. Chervin, and S. Pascarelli, Phys. Rev. Lett. **93**, 255503 (2004).
[6] A. Monza, A. Meffre, F. Baudelet, J.-P. Rueff, M. d'Astuto, P. Munsch, S. Huotari, S. Lachaize, B. Chaudret, and A. Shukla, Phys. Rev. Lett. **106**, 247201 (2011).
[7] J. B. Liu and D. D. Johnson, Phys. Rev. B **79**, 134113 (2009).
[8] K. J. Caspersen, A. Lew, M. Ortiz, and E. A. Carter, Phys. Rev. Lett. **93**, 115501 (2004).
[9] A. Lew, K. Caspersen, E. Carter, and M. Ortiz, J. Mechan. Phys. Solids **54**, 1276 (2006).
[10] R. Taylor, M. Pasternak, and R. Jeanloz, J. Appl. Phys. **69**, 6126 (1991).
[11] P. Toledano, H. Katzke, and D. Machon, J. Phys.: Condens. Matter **22**, 466002 (2010).
[12] K. Takemura, J. Appl. Phys. **89**, 662 (2001).
[13] F. M. Wang and R. Ingalls, Phys. Rev. B **57**, 5647 (1998).
[14] N. Kawamura, N. Ishimatsu, and H. Maruyama, J. Synchrotron Rad. **16**, 730 (2009).
[15] N. Ishimatsu, K. Matsumoto, H. Maruyama, N. Kawamura, M. Mizumaki, H. Sumiya, and T. Irifune, J. Synchrotron Rad. **19**, 0 (2012).
[16] T. Irifune, A. Kurio, S. Sakamoto, T. Inoue, and H. Sumiya, Nature (London) **421**, 599 (2003).
[17] B. Ravel and M. Newville, J. Synchrotron Rad. **12**, 537 (2005).
[18] S. I. Zabinsky, J. J. Rehr, A. Ankudinov, R. C. Albers, and M. J. Eller, Phys. Rev. B **52**, 2995 (1995).
[19] G. Bunker, *Introduction to XAFS* (Cambridge University Press, Cambridge, UK, 2010).
[20] E. Sevillano, H. Meuth, and J. J. Rehr, Phys. Rev. B **20**, 4908 (1979).
[21] V. Iota, J.-H. P. Klepeis, C.-S. Yoo, J. Lang, D. Haskel, and G. Srajer, Appl. Phys. Lett. **90**, 042505 (2007).
[22] W. Bassett and E. Huang, Science **238**, 780 (1987).
[23] C. S. Yadav, G. Seyfarth, P. Pedrazzini, H. Wilhelm, R. Černý, and D. Jaccard, Phys. Rev. B **88**, 054110 (2013).
[24] W. Burgers, Physica (Amsterdam) **1**, 561 (1934).
[25] H.-K. Mao, W. A. Bassett, and T. Takahashi, J. Appl. Phys. **38**, 272 (1967).
[26] The difference of the atomic arrangement between this model and the Burgers model has been illustrated in Figs. 8 and 10 of Ref. [13].
[27] B. Dupé, B. Amadon, Y.-P. Pellegrini, and C. Denoual, Phys. Rev. B **87**, 024103 (2013).
[28] E. Stern, M. Newville, B. Ravel, Y. Yacoby, and D. Haskel, Physica B **208**, 117 (1995).
[29] G. Steinle-Neumann, L. Stixrude, and R. E. Cohen, Proc. Natl. Acad. Sci. USA **101**, 33 (2004).
[30] M. Friák and M. Šob, Phys. Rev. B **77**, 174117 (2008).
[31] V. Thakor, J. B. Staunton, J. Poulter, S. Ostanin, B. Ginatempo, and E. Bruno, Phys. Rev. B **67**, 180405(R) (2003).
[32] R. Cohen and S. Mukherjee, Phys. Earth Planet. Inter. **143**, 445 (2004).
[33] R. Lizárraga, L. Nordström, O. Eriksson, and J. Wills, Phys. Rev. B **78**, 064410 (2008).
[34] S. Merkel, A. F. Goncharov, H.-k. Mao, P. Gillet, and R. J. Hemley, Science **288**, 1626 (2000).